





# Strong Preferential Ion Heating is Limited to within the Solar Alfvén Surface

Justin C. Kasper<sup>1,2</sup>  and Kristopher G. Klein<sup>1,3</sup> <sup>1</sup> Climate and Space Sciences and Engineering, University of Michigan, Ann Arbor, MI 48109, USA<sup>2</sup> Smithsonian Astrophysical Observatory, Cambridge, MA 02138, USA<sup>3</sup> Lunar and Planetary Laboratory, University of Arizona, Tucson, AZ 85719, USA

Received 2019 March 19; revised 2019 April 29; accepted 2019 April 29; published 2019 June 4

## Abstract

The decay of the solar wind helium-to-hydrogen temperature ratio due to Coulomb thermalization can be used to measure how far from the Sun strong preferential ion heating occurs. Previous work has shown that a zone of preferential ion heating, resulting in mass-proportional temperatures, extends about 20–40  $R_{\odot}$  from the Sun on average. Here we look at the motion of the outer boundary of this zone with time and compare it to other physically meaningful distances. We report that the boundary moves in lockstep with the Alfvén point over the solar cycle, contracting and expanding with solar activity with a correlation coefficient of better than 0.95 and with an rms difference of 4.23  $R_{\odot}$ . Strong preferential ion heating is apparently predominately active below the Alfvén surface. To definitively identify the underlying preferential heating mechanisms, it will be necessary to make in situ measurements of the local plasma conditions below the Alfvén surface. We predict that the Parker Solar Probe (PSP) will be the first spacecraft to directly observe this heating in action, but only a couple of years after launch as activity increases, the zone expands, and PSP’s perihelion drops.

*Key words:* solar wind – waves – plasmas – turbulence – Sun: activity

## 1. Introduction

Ions in the solar corona and solar wind are too hot. This has been a puzzle since the start of the space age with the first in situ observations of solar wind plasma by spacecraft. Because electrons carry the heat flux and are the ultimate sink of turbulent energy, one would expect electrons to be hotter than ions, and for this difference to grow more extreme with distance from the Sun; however, ions are hotter in the corona and have similar temperatures to electrons at 1 au. Explaining how ions are heated in the corona and solar wind remains a major challenge in the field. Spectroscopic observations allow us to remotely observe the onset of this preferential ion heating and its consequences. A few tenths of a solar radius  $R_{\odot}$  above the Sun’s photosphere, rising temperatures and falling densities greatly diminish the Coulomb collisions that enforce thermal equilibrium. Unidentified plasma heating mechanisms in this region couple to different ion species with varying degrees of efficiency, preferentially heating some ions more rapidly than others. Extreme differences in ion temperatures develop, with some species reaching temperatures beyond 100 MK (Parker 1988; Kohl et al. 1998; Landi & Cranmer 2009). The ratio of heavy ion species temperature to proton temperature  $T_s/T_p$  is observed to reach and even exceed the mass ratio  $m_s/m_p$ . This suggests a kinetic heating process involving interactions with waves or fluctuations with a characteristic velocity, as ions have equal thermal speeds when they have mass proportional temperatures. Remote observations provide some insight into the mechanisms injecting energy at the base of the corona (McIntosh et al. 2011; Grant et al. 2018). However, these observations are not sufficient to distinguish between the various mechanisms that have been proposed to lead to preferential ion heating throughout the near-Sun environment,

including wave damping, turbulent dissipation, shocks, reconnection, nano-flares, and velocity filtration (see reviews by Ofman 2010; Cranmer 2012; Hansteen & Velli 2012). At some distance, strong preferential ion heating ceases, and ion temperature differences in the solar wind begin to decay with increasing time, as infrequent Coulomb collisions begin to thermalize the plasma (Neugebauer 1976; Hernandez et al. 1987; Tracy et al. 2015). We will refer to the heating process active near the Sun that results in mass proportional, and even super-mass proportional temperatures, as strong preferential heating. In solar wind far from the Sun, mass proportional temperatures are only observed when the frequency of Coulomb collisions is low. Helium and heavier ions in the solar wind with high Coulomb collision rates are at most tens of percent hotter than protons, which is either an indication of the temperature measurement error of the instrument or a sign that only much weaker preferential ion heating occurs in interplanetary space (Maruca et al. 2013; Tracy et al. 2016).

Recently we demonstrated a technique for using solar wind observations at 1 au to determine how far from the Sun the strong preferential ion heating occurs (Kasper et al. 2017, referred to as Paper I). We proposed that there is a zone close to the Sun where ion species experience strong preferential heating, and that within this zone of preferential heating ions reach an equilibrium temperature with an unspecified heating mechanism resulting in different steady temperature ratios for different ion species relative to protons. The start of this zone is seen in the spectroscopic observations just a few  $0.1 R_{\odot}$  above the photosphere. We further assumed that there is an outer boundary of the zone, at a distance  $R_b$  from the Sun, beyond which strong preferential heating ends, and ions are either heated equally or at some much weaker preferential rate. Beyond  $R_b$ , Coulomb relaxation, or the accumulated impact of many small-angle Coulomb scattering interactions between ions, dominates over any weak preferential heating, and will slowly act to drive species toward equal temperatures. For an intuitive sense of this process, consider Spitzer (1962), who



Original content from this work may be used under the terms of the [Creative Commons Attribution 3.0 licence](https://creativecommons.org/licenses/by/3.0/). Any further distribution of this work must maintain attribution to the author(s) and the title of the work, journal citation and DOI.

showed that if two species have a difference in temperature  $\Delta T$  and exchange thermal energy via Coulomb scattering at frequency  $\nu_c$ , with only one species having a notable change in temperature, then the temperature difference will change with time as

$$\frac{d\Delta T}{dt} = -\nu_c \Delta T. \quad (1)$$

Rearranging and defining the temperature excess  $\epsilon \equiv T_\alpha/T_p - 1$ , where  $T_\alpha$  and  $T_p$  are the temperatures of fully ionized helium and hydrogen yields

$$\epsilon(A_c) = \epsilon_o e^{-\int \nu_c dt} = \epsilon_o e^{-A_c} \quad (2)$$

where  $A_c$  is the Coulomb age, or the number of Coulomb thermalization times that have elapsed from when the plasma crossed  $R_b$  to when it was observed in space, and  $\epsilon_o$  is the steady state excess temperature ratio developed below  $R_b$ . Both helium and minor ions seen at 1 au exhibit exponential-like decay in temperature excess with  $A_c$  (Tracy et al. 2015; Kasper et al. 2017). We can locate  $R_b$  by using the exponential decay of  $\epsilon(A_c)$  as a clock to measure the time that it took the solar wind to move from the outer boundary of the zone of preferential heating to the observing spacecraft. In this Letter, we report for the first time the temporal dependence of  $R_b$ , and find that this outer boundary of strong preferential ion heating is well correlated with the Alfvén critical surface. Implications for in situ observations of preferential heating mechanisms are discussed.

## 2. Methodology

This work uses measurements from the Solar Wind Experiment (Ogilvie et al. 1995) and Magnetic Field Investigation (Lepping et al. 1995) instruments on the NASA Wind spacecraft. The same data selection criterion were used as were presented in Paper I with the added exclusion of data collected prior to 1997 October 27. Before this date, a different observation mode yielded larger measurement uncertainties for  $T_\alpha$ .

Our model for  $A_c$  and  $R_b$  uses radial power-law exponents  $\delta$  and  $\sigma$  to capture how overall temperature and speed vary with distance from the Sun,  $T(r) = T_0 (r/R)^{-\delta}$  and  $U(r) = U_0 (r/R)^{-\sigma}$ . The solar wind proton density and magnetic field amplitude scale as

$$n_p(r) = n_0 R^{2-\sigma} r^{\sigma-2} \quad (3)$$

and

$$B(r) = B_0 R^2 r^{-2} \sqrt{1 + \omega^2 r^{2+2\sigma} U_0^{-2} R^{-2\sigma}}, \quad (4)$$

where the angular frequency of the Sun's rotation in the equatorial plane is  $\omega = 2.7 \times 10^{-6} \text{ rad s}^{-1}$ . Quantities with a subscript 0 are values measured at  $R = 1 \text{ au}$ .

Our full model for  $\epsilon(A_c)$  is more complicated than Equation 2 because it allows both species' temperatures to change, with the relative rates of heating and cooling determined by the relative mass density  $F \equiv m_\alpha n_\alpha / m_p n_p$ . An increase in  $F$  causes a faster equalization of  $T_p$  and  $T_\alpha$ . We also account for the variation of  $\nu_c$  due to these relative temperatures changing with distance; see Equation (11) in Paper I for the full expression.

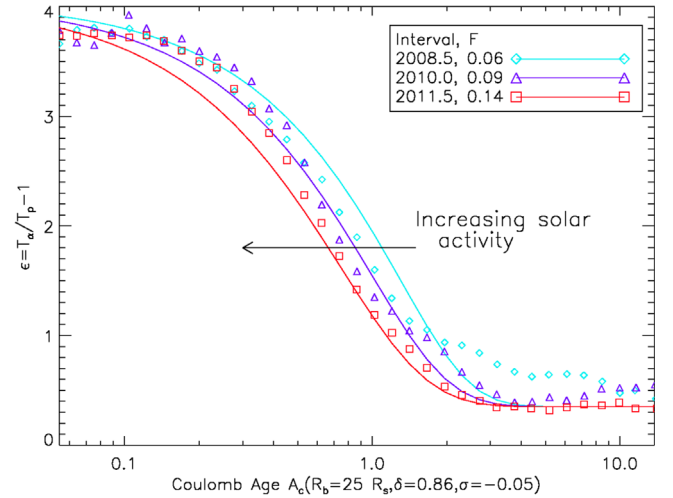


**Figure 1.** Observed  $\epsilon(A_c)$  for three 1.5 year intervals with increasing solar activity (colored symbols). Solid lines are predicted  $\epsilon(A_c)$  for each interval, factoring in the increasing observed mass density ratio  $F$  but holding  $R_b = 25 R_\odot$ . At solar minimum,  $25 R_\odot$  is an overestimate of  $R_b$ , with the observed  $\epsilon$  decaying faster than the model. As activity increased  $R_b$  is underestimated, suggesting it is moving outward from the Sun.

In Paper I, we used a range of  $\delta$  that bracketed published values seen by *Helios* (Marsch et al. 1982; Hellinger et al. 2011) and assumed  $\sigma$  was zero. A best fit for observed  $\epsilon$  as a function of  $A_c$ , with  $R_b$  and  $\epsilon_o$  as free parameters was found. The analysis in Paper I and in this work is limited to solar wind intervals where the speed is between  $300$  and  $500 \text{ km s}^{-1}$  to ensure good data coverage of both high and low collisional age plasma. Using all solar wind speeds does not qualitatively affect the results presented here. Over the entire Wind mission the model fits the observations with a Pearson's chi-squared test of  $\chi^2/\text{dof}$  of less than 2, and can predict the mean  $\epsilon$  for a given  $A_c$  with an rms error of less than 10%. If  $\delta$  is specified, the best fit uncertainty in  $R_b$  is much less than one  $R_\odot$ . For every 0.1 increase in  $\delta$ ,  $R_b$  drops  $8.8 R_\odot$  closer to the Sun. For the range of  $\delta$  reported in the literature  $R_b$  could be between 20 and  $40 R_\odot$ .

## 3. Results

Temporal variation in  $\epsilon(A_c)$  and the outer boundary  $R_b$  can be seen in a relatively raw view of the observations. Figure 1 compares the observed  $\epsilon(A_c)$  (symbols) with the expected decay (lines) if  $R_b$  is taken to be constant but the mass density ratio  $F$  is updated to account for its observed solar cycle dependence. Over these three 1.5 yr intervals  $F$  grows from 0.06 to 0.14 (Kasper et al. 2012), and with more helium, the two species can reach thermal equilibrium faster. Most of the observations fall below the curve in solar minimum (light blue diamonds), and are generally all above the curve as activity increases (red squares). This can be explained as an underestimate of  $A_c$  in solar minimum because  $R_b$  is closer to the Sun than we assumed, and an overestimate of  $A_c$  in times of high activity because  $R_b$  has moved closer to the observer than assumed. The elevated  $\epsilon$  at large  $A_c$  in 2008 appears to be due a higher uncertainty in the temperature of helium caused by lower helium densities, which does not impact this analysis.

We next calculate a best-fit value for  $R_b$  as a function of year over the entire Wind mission, and compare it to a proxy for solar activity and to several critical surfaces surrounding the Sun, where the bulk solar wind speed transitions from below to

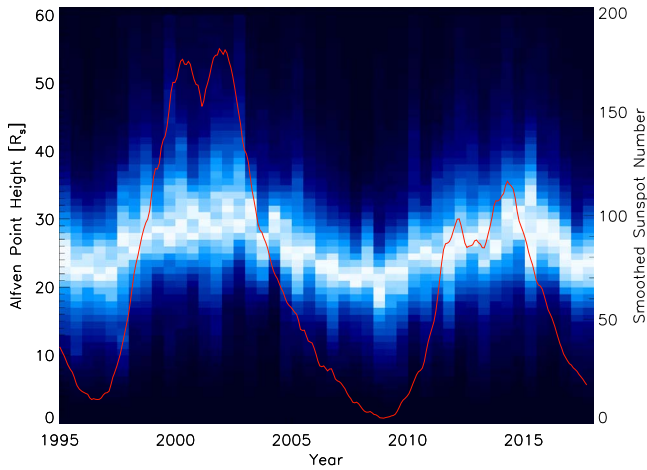


**Figure 2.** 2D histogram of the height of the Alfvén surface  $R_A$  over time calculated using millions of individual measurements of the solar wind at 1 au (shades of blue) along with the smoothed sunspot number (red line).

above some characteristic wave speed. It is also known that critical surfaces around the Sun have temporal dependencies associated with the solar cycle (Katsikas et al. 2010). We focus on two of these surfaces, related to two fundamental wave speeds in a magnetized plasma, the Alfvén speed  $v_A$  and the sound speed  $v_s$ . For a radial solar wind profile  $U(r)$  the radial location of the Alfvén and sound critical surfaces,  $R_A$  and  $R_s$ , are where  $v_A(r) = U(r)$  and  $v_s(r) = U(r)$ . Beyond these critical surfaces, an Alfvén or sound wave, respectively, cannot travel back to the Sun. The Alfvén speed is calculated as

$$v_A(r) = \frac{B(r)}{\sqrt{4\pi n_p(r) m_p}}. \quad (5)$$

Using an Alfvén speed with only the proton mass density or the total ion mass density does not significantly alter the results presented below. For the sound critical surface  $R_s$ , we use Equation (11) from Katsikas et al. (2010) evaluated at equatorial latitudes. For each measurement at 1 au, assuming a particular radial scaling for the solar wind temperature ( $\delta$ ) and velocity ( $\sigma$ ), we determine  $R_A$  and  $R_s$ . The distribution of  $R_A$  as a function of time is shown in Figure 2 as a column-normalized 2D histogram;  $R_A$  typically has values around  $25 R_\odot$  with significant expansion and contraction between solar minimum and solar maximum.

The outer boundary of the zone of preferential heating  $R_b$  is calculated using the same scheme as in Paper I, except instead of segregating by solar wind speed, the data is subdivided into 1.5 year intervals. The mean value of  $R_b$  as a function of time from 1998 to 2017 is plotted in Figure 3 for values for radial scalings of proton temperature and speed consistent with previous measurements of the solar wind, ( $\delta = 0.814$  and  $\sigma = -0.05$ , see Hellinger et al. 2011, 2013). We observe significant variation in  $R_b$ , ranging from  $\sim 10 R_\odot$  at solar minimum to  $\sim 35 R_\odot$  at solar maximum. This variation occurs for both the relatively strong Cycle 23 and the weaker Cycle 24. The  $1\sigma$  error in  $R_b$  is quite narrow, on the order of  $0.5 R_\odot$ . To compare with  $R_b$ , we also calculate average values and rms variations of  $R_A$  and  $R_s$ , plotted in red and blue in Figure 3. The sound critical surface  $R_s$  is much closer to the Sun than  $R_b$  and does not have the same temporal variation with solar activity. The Alfvén critical surface’s temporal variation is well

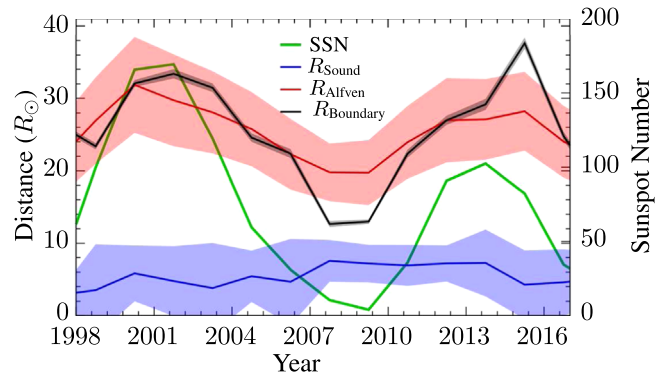


**Figure 3.** Comparison of the motion of the outer boundary  $R_b$  of the zone of preferential ion heating (black) with the sound surface  $R_s$  (blue) and Alfvén surface  $R_A$  (red) as a function of time for  $\delta = 0.814$  and  $\sigma = -0.05$ . The width of the line for  $R_b$  indicates the uncertainty from the model’s fit. The red and blue shaded regions indicate the rms variation of  $R_s$  and  $R_A$  about their means. The yearly averaged sunspot number (green) is also shown.

correlated with  $R_b$ , with an rms difference between the two distances of less than  $4.23 R_\odot$  and a Spearman rank correlation of 0.956 with a significance of  $3 \times 10^{-6}$ . The correlation is significantly better than with sunspot number, a typical indicator of solar activity (0.842), or the sound surface ( $-0.367$ ).

Another physically meaningful distance is where the ratio of thermal and magnetic pressures,  $\beta(r) = 8\pi n_p(r) k_B T_p(r) B(r)^{-2}$ , crosses some critical value; we denote this surface as  $R_\beta$ . Choosing different critical  $\beta$  values of less than unity, we find that  $R_\beta$  and  $R_b$  are well correlated, with a Spearman rank correlation coefficient of 0.820, though not as well correlated as  $R_b$  and  $R_A$ . Using standard minimization techniques, we determine that a critical  $\beta$  value of 0.023 has the smallest rms distance between  $R_b$  and  $R_\beta$ . We note, however, that this may be a transitive effect; the mean value of  $\beta$  at  $R_A$  is approximately 0.03, with only minimal temporal variation. Therefore, as  $R_b$  is correlated with  $R_A$  and  $\beta(R_A) \approx 0.03$ , we expect that the distance  $R(\beta \approx 0.03)$  will be correlated with  $R_b$ .

We repeat the process of calculating  $R_b$ ,  $R_A$ ,  $R_s$ , and  $R_\beta$  for a range of radial power-law exponents for proton temperature and speed,  $\delta \in [0.75, 0.95]$  and  $\sigma \in [-0.1, 0]$ , compatible with radial trends extracted from *Helios*. The Spearman rank correlation coefficients between  $R_b$  and the three critical surfaces have little variation due to the power-law exponents (not shown); for all values of  $\delta$  and  $\sigma$  considered,  $R_A$  is by far the best-correlated surface. Further, we find that there is neither any meaningful global minimum value for  $\delta$  and  $\sigma$  in the rms difference between  $R_b$  and  $R_A$ ,  $\Delta R_{A,b}$  nor is there any global maximum for their correlation coefficient. Rather, there is a family of solutions for which  $\Delta R_{A,b}$  is minimized. Specifically, there is a unique value of  $\delta$  for any  $\sigma$  resulting in a minimum  $\Delta R_{A,b}(\sigma, \delta)$  of  $\lesssim 5 R_\odot$ , as illustrated in Figure 4. The  $\delta$  leading to the minimum  $\Delta R_{A,b}$  obeys the equation  $\delta = 0.813 - 1.037\sigma$ . These preferred solutions follow closely, but are not identical to the  $\delta = 2/3 - 4/3\sigma$  scaling suggested by the radial dependence of the collisional age integral discussed in Paper I. The minor disagreement between these trends is likely caused by uncertainty introduced by our model for radial variation in densities and Alfvén speeds. Venzmer & Bothmer (2018) have produced limits on values for  $\sigma$  and  $\delta$  based upon recent analysis of *Helios* radial trends that bound the  $\Delta R_{A,b}$  minimum extracted from the outer boundary analysis. Using

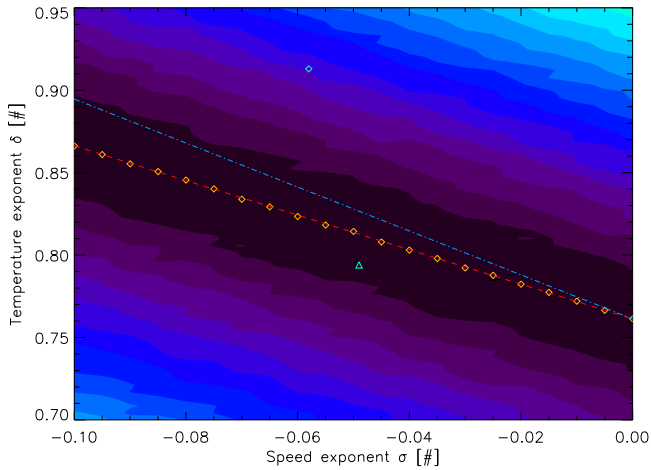


**Figure 4.** The rms difference between zone boundary  $R_b$  and Alfvén point  $R_A$ ,  $\Delta R_{A,b}$ , as a function of radial exponents  $\sigma$  for speed and  $\delta$  for temperature. Published values for  $\sigma$  in steady solar wind are generally between  $-0.1$  and  $0$ . Color contours indicate  $1 R_\odot$  steps in the rms difference, with the minimum values indicated by the orange diamonds. The red line indicates the best fit of relation between  $\sigma$  and  $\delta$  that passes through the rms minimum. The blue line is a prediction of this relation based on the degeneracy between two exponents in our equation for  $A_c$ . This analysis results in the prediction that  $\sigma$  and  $\delta$  fall on the red line. Points from Venzmer & Bothmer (2018) indicate values from two recent analyses of *Helios* radial trends.

the mean value from that study,  $\sigma = -0.05$ , we predict that  $\delta = 0.85$ .

#### 4. Discussion

These results suggest that the outer boundary of the zone of strong preferential ion heating  $R_b$  is the Alfvén critical surface  $R_A$ , and that the zone and the Alfvén surface expand in lockstep as solar activity changes. This leads to the question of why any preferential heating mechanism would be affected by a transition across this surface. In the expanding solar wind, some fraction of outward propagating wave power is reflected back toward the Sun due to large-scale gradients in background quantities. Below  $R_A$ , these waves can travel all the way back to the Sun and interact with outward propagating waves, leading to wave-reflection-driven turbulence (Matthaeus et al. 1999; Perez & Chandran 2013). Above  $R_A$ , backward-propagating waves in the plasma frame are advected forward in the Sun’s reference frame. The abundance of counter-propagating waves below  $R_A$  can dramatically enhance local preferential ion heating, either due to wave-particle interactions (Kasper et al. 2013) or alterations to the background turbulence (Velli et al. 1989; Matthaeus et al. 1999; Dmitruk et al. 2001; Cranmer et al. 2007; Verdini & Velli 2007; Chandran & Hollweg 2009; Verdini et al. 2012). No theoretical predictions of dissipation have suggested a sharp change in the preferential heating exactly at  $R_A$ . Like crossing the event horizon of a black hole, there is no sudden change experienced when crossing  $R_A$ , even as the plasma becomes causally disconnected from the Sun. While it is possible that there is a discrete termination of preferential heating mechanisms, it is more likely that the preferential heating gradually shuts off after the plasma passes  $R_A$ . Given that we find  $\Delta R_{A,b}$  to always be greater than  $\approx 5 R_\odot$ , this difference may serve as a estimate for the thickness over which the preferential heating ceases.

Could there be some form of discontinuity or transition at the Alfvén point? Weber & Davis (1967) proposed that the corona

co-rotates with the Sun out to the Alfvén point, with a sudden drop in rotational speed as the solar wind Alfvén Mach number exceeds unity. Perhaps the diminished role of magnetic tension and the rotation of the magnetic field either alters the local turbulence or enhances reflection back toward the Sun. Remote observations where the solar wind transitions character from striated to flocculated (DeForest et al. 2016) report distances of  $44\text{--}88 R_\odot$ , which is slightly beyond  $R_A$ , indicating that this transition region is not co-terminous with  $R_b$ . The Alfvén surface has been identified in numerical magnetohydrodynamic (MHD) simulations (Chhiber et al. 2018) as the region where large-scale MHD turbulence first manifests, potentially changing the mechanisms heating the plasma.

We emphasize that we are only predicting that strong preferential ion heating shuts off beyond  $R_A$ , not that all ion heating is terminated outside of this zone. Weak preferential heating of minor ions may also continue outside of this zone, leading to no more than a 10 percent difference between proton and alpha temperature, as reported for highly collisional solar wind at 1 au (Maruca et al. 2013; Tracy et al. 2016); this temperature difference between species is also consistent with the temperature measurement error of the particle instruments (Kasper et al. 2006).

The Parker Solar Probe (PSP), launched in 2018 August, is the first spacecraft to enter the near-Sun environment, with an initial perihelion of  $35 R_\odot$  in 2018 and final perihelia of  $9.86 R_\odot$  starting in 2024 (Fox et al. 2016). The first scientific objective of PSP is to “trace the flow of energy that heats and accelerates the solar corona and solar wind” (Fox et al. 2016, p. 4) By closing to within  $10 R_\odot$  of the Sun’s surface, PSP will have a high probability of observing nonthermal heating in action with its electromagnetic field (Bale et al. 2016) and ion and electron plasma (Kasper et al. 2016) instruments. The explicit assumption has been that we are much more likely to observe this heating in action below the Alfvén point because we are in the magnetic atmosphere of the Sun, casually connected to the Sun, or simply because it may be easier to map the plasma to its sources that close to the Sun.

With the results reported here we can make a specific prediction for how PSP may observe and reveal preferential ion heating in action, and the underlying physics, for the first time. We have found that not only is there a zone of preferential ion heating surrounding the Sun that extends tens of  $R_\odot$  from the Sun, but also that the outer boundary  $R_b$  of this zone expands with solar activity, closely tracking the location of the Alfvén surface and likely intimately connected to changes in the nature of the plasma and waves across this surface. Using Wind observations, in Figure 5 we advance our calculation of  $R_b$  by 11 and 22 yr to project forward data from the last two solar cycles into the PSP mission timeframe. Against this projection we plot the minimum distance of approach to the Sun by PSP, which steps closer to the Sun via six Venus gravity assists. We find that at launch in solar minimum, PSP’s perihelion is too high, and  $R_b$  is too low, for PSP to enter the zone. However, in late 2020 as PSP’s perihelion lowers, the preferential heating zone and the Alfvén point will extend outward and cross the trajectory of the spacecraft. This prediction varies slightly when using  $R_b$  from the relatively strong Cycle 23 or the weaker Cycle 24. See also Chhiber et al. (2019) for a discussion of predictions from global MHD simulations for the Alfvén critical surface.

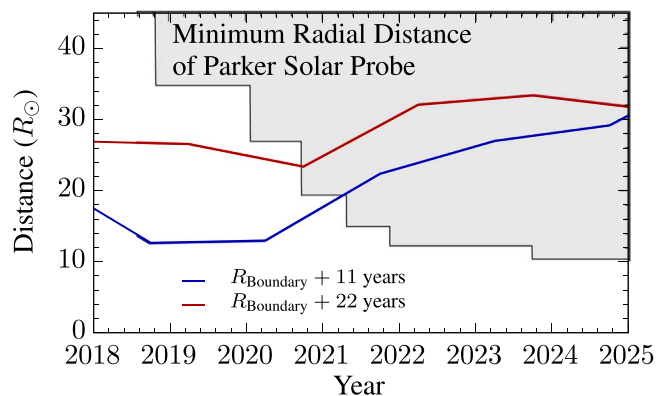


**Figure 5.** Location of  $R_b$  calculated from Wind observations, advanced 11 and 22 yr in time in order to predict the motion of the outer boundary during the Parker Solar Probe (PSP) mission. While PSP starts with a perihelion above  $R_b$ , we suggest that the spacecraft and boundary will cross in late 2020, permitting the first direct observations of preferential ion heating.

As  $R_b$  rarely exceeds  $35 R_\odot$ , it is likely that no previous spacecraft has sampled this region of preferential heating. As PSP approaches the zone, the derived distance to  $R_b$  calculated using the method described in this work should decrease. By comparing local measurements of the Alfvén speed and the solar wind bulk speed, we should be able to determine when PSP crosses the Alfvén point. At that point we predict PSP will be able to detect if  $\epsilon$  has reached its expected asymptotic value as well as signatures local heating processes in this region. By doing so, PSP should be able to fulfill its first scientific objective of characterizing how the solar corona and solar wind are heated.

All underlying data used for this analysis are archived and available for download at the NASA Space Physics Data Facility (<https://spdf.gsfc.nasa.gov/>). We thank Tristan Weber for initial calculations of the Alfvén surface over time. J.C.K. is supported by Wind grant NNX14AR78G. K.G.K. is supported by NASA HSR grant NNX16AM23G.

#### ORCID iDs

Justin C. Kasper  <https://orcid.org/0000-0002-7077-930X>

Kristopher G. Klein  <https://orcid.org/0000-0001-6038-1923>

#### References

- Bale, S. D., Goetz, K., Harvey, P. R., et al. 2016, *SSRv*, 204, 49
- Chandran, B. D. G., & Hollweg, J. V. 2009, *ApJ*, 707, 1659
- Chhiber, R., Usmanov, A. V., DeForest, C. E., et al. 2018, *ApJL*, 856, L39
- Chhiber, R., Usmanov, A. V., Matthaeus, W. H., & Goldstein, M. L. 2019, *ApJS*, 241, 11
- Cranmer, S. R. 2012, *SSRv*, 172, 145
- Cranmer, S. R., van Ballegoijen, A. A., & Edgar, R. J. 2007, *ApJS*, 171, 520
- DeForest, C. E., Matthaeus, W. H., Viall, N. M., & Cranmer, S. R. 2016, *ApJ*, 828, 66
- Dmitruk, P., Milano, L. J., & Matthaeus, W. H. 2001, *ApJ*, 548, 482
- Fox, N. J., Velli, M. C., Bale, S. D., et al. 2016, *SSRv*, 204, 7
- Grant, S., Jess, D., Zaqarashvili, T., et al. 2018, *NatPh*, 14, 480
- Hansteen, V. H., & Velli, M. 2012, *SSRv*, 172, 89
- Hellinger, P., Matteini, L., Štverák, Š., Trávníček, P. M., & Marsch, E. 2011, *JGRA*, 116, 9105
- Hellinger, P., Trávníček, P. M., Štverák, Š., Matteini, L., & Velli, M. 2013, *JGRA*, 118, 1351
- Hernandez, R., Livi, S., & Marsch, E. 1987, *JGR*, 92, 7723
- Kasper, J. C., Abiad, R., Austin, G., et al. 2016, *SSRv*, 204, 131
- Kasper, J. C., Klein, K. G., Weber, T., et al. 2017, *ApJ*, 849, 126
- Kasper, J. C., Lazarus, A. J., Steinberg, J. T., Ogilvie, K. W., & Szabo, A. 2006, *JGRA*, 111, A03105
- Kasper, J. C., Maruca, B. A., Stevens, M. L., & Zaslavsky, A. 2013, *PhRvL*, 110, 091102
- Kasper, J. C., Stevens, M. L., Korreck, K. E., et al. 2012, *ApJ*, 745, 162
- Katsikas, V., Exarhos, G., & Moussas, X. 2010, *AdSpR*, 46, 382
- Kohl, J. L., Noci, G., Antonucci, E., et al. 1998, *ApJL*, 501, L127
- Landi, E., & Cranmer, S. R. 2009, *ApJ*, 691, 794
- Lepping, R. P., Acuña, M. H., Burlaga, L. F., et al. 1995, *SSRv*, 71, 207
- Marsch, E., Schwenn, R., Rosenbauer, H., et al. 1982, *JGR*, 87, 52
- Maruca, B. A., Bale, S. D., Sorriso-Valvo, L., Kasper, J. C., & Stevens, M. L. 2013, *PhRvL*, 111, 241101
- Matthaeus, W. H., Zank, G. P., Oughton, S., Mullan, D. J., & Dmitruk, P. 1999, *ApJL*, 523, L93
- McIntosh, S. W., de Pontieu, B., Carlsson, M., et al. 2011, *Natur*, 475, 477
- Neugebauer, M. 1976, *JGR*, 81, 78
- Ofman, L. 2010, *LRSP*, 7, 4
- Ogilvie, K. W., Chornay, D. J., Fritzenreiter, R. J., et al. 1995, *SSRv*, 71, 55
- Parker, E. N. 1988, *ApJ*, 330, 474
- Perez, J. C., & Chandran, B. D. G. 2013, *ApJ*, 776, 124
- Spitzer, L. 1962, *Physics of Fully Ionized Gases* (New York: Interscience)
- Tracy, P. J., Kasper, J. C., Raines, J. M., et al. 2016, *PhRvL*, 116, 255101
- Tracy, P. J., Kasper, J. C., Zurbuchen, T. H., et al. 2015, *ApJ*, 812, 170
- Velli, M., Grappin, R., & Mangeney, A. 1989, *PhRvL*, 63, 1807
- Venzmer, M. S., & Bothmer, V. 2018, *A&A*, 611, A36
- Verdini, A., Grappin, R., Pinto, R., & Velli, M. 2012, *ApJL*, 750, L33
- Verdini, A., & Velli, M. 2007, *ApJ*, 662, 669
- Weber, E. J., & Davis, L., Jr. 1967, *ApJ*, 148, 217